Int. J. Heat Mass Transfer. Vol. 33, No. 10, pp. 2161–2172, 1990
Printed in Great Britain

0017–9310/90 $3.00 + 0.00

Buoyancy induced instability of laminar flows in vertical annuli—II. Model development and analysis

DASARI V. RAO and MOHAMED S. EL-GENK

Department of Chemical and Nuclear Engineering, The University of New Mexico, Albuquerque, NM 87131, U.S.A.

(*Received* 11 *April* 1989 *and in final form* 11 *December* 1989)

Abstract—A two-dimensional numerical model, based on the elliptic Navier–Stokes equations, is developed to predict the location of incipient instability, x_{fr}, in low Reynolds number water flows in vertical annuli. Results show that neglecting the radial momentum can underpredict the values of x_{fr} at high Gr_q/Re values by as much as 45%. Conversely, the axial momentum diffusion only insignificantly affects the velocity fields and, hence, the accuracy of predicting x_{fr}. The results of a parametric analysis investigating the effects of various operating conditions and geometrical parameters is used to develop general criteria for predicting the onset of flow instability in vertical annuli. These criteria are within ±10 and ±15% of the experimental data for buoyancy assisted and opposed flows, respectively.

INTRODUCTION

CHARACTERIZATION of heat transfer to low Reynolds number flows in vertical channels is complicated by the introduction of buoyant forces at high heat flux-to-mass flow ratios (Gr_q/Re). At higher Gr_q/Re values, the variations in fluid viscosity and density across the boundary layer become sufficiently large, causing significant distortion in the velocity fields and initiating transition from stable laminar flow to turbulent flow [1, 2]. Such transition enhances the rates of heat transfer downstream of the *location of incipient instability*, also referred to as the *location of incipient flow transition*, x_{fr} [3, 4].

Numerous experimental and theoretical studies investigating the transition from stable laminar flow to buoyancy induced turbulent flow have been reported for pipes [2, 3, 5–7], channels formed by parallel plates [8, 9], rod bundles [10, 11], and vertical annuli [4, 14, 15]. The theoretical investigations of buoyancy induced instability have only focused on relating the conditions for onset of transition to the magnitude of the distortion in the axial velocity profile. The axial location of incipient instability was taken to be equal to that at which both the radial gradient of the axial velocity and the axial velocity corresponding to some radial coordinate vanish. However, the accuracy of this criterion depends on the accuracy of calculating the axial velocity profiles upstream of x_{fr}.

Most studies have either assumed fully developed flow [12, 13] or employed the boundary layer approximation [14, 15] to calculate the axial velocity profile upstream of x_{fr}. Sherwin [12] obtained an estimate for minimum Gr_q/Re values required to initiate transition using the fully developed flow approximation. The validity of this approximation is limited to very long test sections and low values of Gr_q/Re. El-Shaarawi and Sharan [15] solved the constant property boundary layer equations to predict x_{fr} for laminar upflow of air in a vertical annulus with an isothermal inner wall. Similar equations were solved by Sherwin and Wallis [14] to predict x_{fr} for laminar downflow of water in a vertical annulus with an isoflux inner wall. Although good agreements were reported between the boundary layer solution and the experimental data at low Gr_q/Re values [14], theoretical predictions were consistently lower at higher Gr_q/Re values. A similar trend was also reported for laminar upflow in tubes [6]. This disagreement between the experimental data and the boundary layer solution at higher Gr_q/Re values can be attributed to the following simplifying assumptions in the boundary layer approach: radial momentum transfer is negligible ($\partial p/\partial r = 0$), axial diffusion of momentum is negligible, and the fluid properties except for density are temperature independent.

To account for these shortcomings of the boundary layer approximation, this research developed a numerical model that solves the complete set of elliptic Navier–Stokes equations with temperature dependent fluid properties. The accuracy of the model was verified by comparing the model predictions of x_{fr} with the experimental data of ref. [4] for both buoyancy assisted and opposed flows and those of ref. [14] for downflow of water in vertical annuli. Effects of radial momentum transfer and axial diffusion on x_{fr} were quantified by comparing the model predictions based on elliptic governing equations with those obtained, as a part of the study, using the parabolic form of governing equations and the boundary layer equations. To examine the effect of inlet parameters, oper-

NOMENCLATURE

A_c	cross sectional flow area [m^2]
C_p	specific heat [kJ kg^{-1}]
D	diameter [m]
D_e	equivalent hydraulic diameter, $D_o - D_i$ [m]
g	acceleration due to gravity, 9.81 m s^{-2}
Gr_q	Grashof number, $g\beta D_e^4 q/\nu^2 k$
k	thermal conductivity [W m^{-1} K^{-1}] or index used in equations (7)–(11)
l	index used in equations (7)–(11)
L	length of the heated section [m]
L_{nh}	length of non-heated calming section (D_e)
m	number of sweep
$\dot{m}$	mass flow through the annulus [kg s^{-1}]
Nu	Nusselt number, $qD_e/k(t_w - t_b)$
p	pressure [Pa]
P	dimensionless pressure, $p/\rho u_{in}^2$
Pe	Peclet number, $Re \cdot Pr$
Pr	Prandtl number, $\mu C_p/k$
q	surface heat flux [kW m^{-2}]
Q	dimensionless heat flux, $qr_e/k(t_{sat} - t_{in})$
r	radial location or radius [m]
R	dimensionless radial location, $(r - r_i)/(r_o - r_i)$
ΔR	radial step width
Re	Reynolds number, $\dot{m}D_e/A_c\mu$
t	temperature [K]
T	dimensionless temperature, $(t - t_{in})/(t_{sat} - t_{in})$
u	axial velocity [m s^{-1}]
U	dimensionless axial velocity, u/u_{in}
v	radial velocity [m s^{-1}]
V	dimensionless radial velocity, v/v_{in}
x	axial distance measured from the entrance of the heated section in the direction of the flow [m]
X	dimensionless axial distance, x/D_e
ΔX	axial step width.

Greek symbols

β	coefficient of volumetric expansion [K^{-1}]
ε	annulus ratio, D_o/D_i
μ	dynamic viscosity of water [kg m^{-2} s^{-1}]
ν	kinematic viscosity [m^2 s^{-1}]
ρ	density of water [kg m^{-3}]

Subscripts

b	water bulk temperature
cr	critical value
fr	location of incipient instability
i	inner heated stainless steel tube
in	inlet of the test section
max	maximum axial velocity
o	outer wall of the annulus
sat	saturation (or boiling point)
w	heated wall.

ating parameters, geometrical parameters and surface heat flux on x_{fr}, a parametric analysis was conducted. Based on the results of the parametric analysis as well as the experimental data [4, 14], a general criteria for the onset of flow instability in both buoyancy assisted and opposed flow of water in vertical annuli were developed. The next two sections describe the governing equations of the model and the numerical scheme used in solving these equations.

PHYSICAL MODEL

The problem under consideration is that of a steady, two-dimensional, axisymmetric, developing laminar flow of water in vertical concentric–circular annuli. These annuli have a uniformly heated inner wall and an insulated outer wall. The basic case analysis assumed uniform fluid velocity and temperature at the inlet of the test section. Because of the large temperature variation across the annular gap at high Gr_q/Re values, the model treats the fluid viscosity as temperature dependent, while the variations in fluid density were handled using the Boussinesq approximation. The steady-state governing equations and the boundary conditions, in their conservative form, are given below.

Governing equations

(a) Continuity

$$\frac{\partial(\rho U)}{\partial X} + \frac{1}{R}\frac{\partial(\rho RV)}{\partial R} = 0. \tag{1}$$

(b) Axial momentum

$$\frac{\partial UU}{\partial X} + \frac{1}{R}\frac{\partial(RUV)}{\partial R} = -\frac{\partial P}{\partial X} + \frac{Gr_q T}{4Q\,Re^2} + \left[\frac{1}{R}\frac{\partial}{\partial R}\left(\frac{2R}{Re}\frac{\partial U}{\partial R}\right) + \frac{\partial}{\partial X}\left(\frac{2}{Re}\frac{\partial U}{\partial X}\right)\right]. \tag{2}$$

(c) Radial momentum

$$\frac{\partial(UV)}{\partial X} + \frac{1}{R}\frac{\partial}{\partial R}(RVV) = -\frac{\partial P}{\partial R} + \left[\frac{\partial}{\partial R}\left(\frac{2}{Re\,R}\frac{\partial RV}{\partial R}\right)\right]. \tag{3}$$

(d) Energy

$$\frac{\partial(UT)}{\partial X} + \frac{1}{R}\frac{\partial(RVT)}{\partial R} = \left[\frac{1}{R}\frac{\partial}{\partial R}\left(\frac{2R}{Pr}\frac{\partial T}{\partial R}\right)\right]. \tag{4}$$

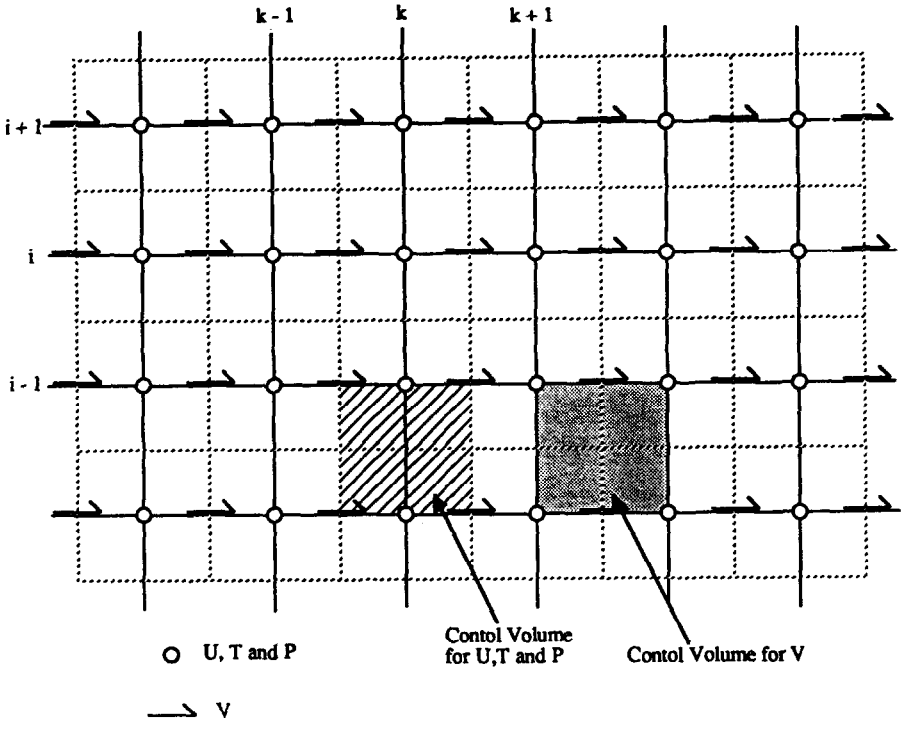

FIG. 1. Staggered grid used to discretize the governing equations.

(e) Integral continuity

$$\int_0^1 \rho UR \, dR = \tfrac{1}{2}\rho_{in}\left(\frac{\varepsilon+1}{\varepsilon-1}\right). \quad (5)$$

Boundary conditions

$U = 1.0$, $V = 0$, and $T = 0$

$$@\ X = 0 \text{ (entrance)} \quad (6')$$

$U = 0$, $V = 0$, and $\partial T/\partial R = -Q_i(X)$

$$@\ X > 0; \quad R = 0 \text{ (inner wall)} \quad (6'')$$

$U = 0$, $V = 0$, and $\partial T/\partial R = 0$

$$@\ X > 0; \quad R = 1 \text{ (outer wall)}. \quad (6''')$$

To assess the effects of axial diffusion and radial momentum transfer on the accuracy of the model predictions for x_{fr}, the model results for three cases, each representing a set of simplifying assumptions, were compared with the experimental data. In case I, the governing equations in their present form (equations (1)–(6)) were solved, while in case II the parabolic form of the governing equations, obtained by neglecting the axial diffusion term in equation (2), were solved. Case III assumed a boundary layer flow and the velocity and temperature profiles were obtained from the solution of the boundary layer equations. These equations were deduced from equations (1)–(5) by neglecting radial momentum transfer (equation (3)) and axial diffusion (last term in equation (2)).

The governing equations for each of these cases, subjected to the prescribed boundary conditions (equation (6)), were solved for the velocity and the temperature profiles as functions of the axial location. The axial location of incipient instability, x_{fr}, was defined as that where the axial velocity as well as the radial gradient of the axial velocity near one of the walls vanish ($U = 0$ and $\partial U/\partial R \approx 0$; @ $R = 0$ for downflow or @ $R = 1$ for upflow). Because the analytical solution of equations (1)–(6) was unattainable a numerical scheme, outlined in the following section, was employed to solve these equations for all three cases.

NUMERICAL SCHEME

Although several numerical schemes have been proposed to solve the elliptic form of Navier–Stokes equations [16, 17], they are not adoptable to the present problem because they require specification of the entire domain of interest and the outflow boundary conditions a priori. In the present problem because x_{fr} is not known beforehand neither of these requirements could be met. The proposed numerical scheme employed an iterative, marching, finite difference scheme, which is similar to that proposed by Patankar and Spalding [18] for solving the parabolic transport equations. In addition, the current scheme solves the axial diffusion terms in equation (2) ($\partial^2 U/\partial X^2$) using a special first-order finite differencing scheme; higher order of accuracy was obtained by incorporating additional sweeps of the calculation domain.

The proposed numerical scheme divided the cal-

culation domain ($0 \leqslant R \leqslant 1$ and $0 \leqslant X \leqslant X_{fr}$) into several control volumes using a staggered grid structure [19] (see Fig. 1). The governing equations (equations (1)–(6)) were then reduced to a set of linearized finite difference equations by integrating them over the respective control volumes.

(a) Continuity equation

$$a_j^c V_{i,j-1} + b_j^c V_{i,j} + c_j^c V_{i,j+1} = y_j^c; \quad \text{for } j = 2, n$$

$$V_{i,j} = 0; \quad \text{for } j = 1 \text{ and } n+1. \tag{7}$$

(b) Axial momentum equation

$$a_k^u U_{i,k-1} + b_k^u U_{i,k} + c_k^u U_{i,k+1} = -\partial P/\partial X_i + y_k^u; \quad \text{for } k = 2, n$$

$$U_{i,k} + U_{i,k-1} = 0; \quad \text{for } k = 2 \text{ and } n+2. \tag{8}$$

(c) Radial momentum equation

$$a_j^v V_{i,j-1} + b_j^v V_{i,j} + c_j^v V_{i,j+1} = -(P_k - P_{k-1})/\Delta R + y_j^v; \quad \text{for } j = 2, n$$

$$V_{i,j} = 0; \quad \text{for } j = 1 \text{ and } n+1 \text{ and } P_k - P_{k-1} = 0; \quad \text{for } k = 2 \text{ and } n+2. \tag{9}$$

(d) Energy equation

$$a_k^t T_{i,k-1} + b_k^t T_{i,k} + c_k^t T_{i,k+1} = y_k^t; \quad \text{for } k = 2, n$$

$$T_{i,k} - T_{i,k+1} = Q(\Delta R); \quad \text{for } k = 1 \text{ and } T_{i,k} - T_{i,k-1} = 0; \quad \text{for } k = n+2$$

$$T_{i,k} - T_{i,k-1} = 0; \quad \text{for } k = n+2 \text{ (at the outer wall).} \tag{10}$$

(e) Integral continuity equation

$$\left(\frac{\varepsilon+1}{\varepsilon-1}\right) = (\Delta R)\left[\sum_{j=1}^{n} (f_j + f_{j-1})\right]$$

$$\text{where} \quad f_j = \frac{(\rho UR)_j}{\rho_{in}}. \tag{11}$$

The coefficients a_l^ϕ, b_l^ϕ, c_l^ϕ, and y_l^ϕ ($l = j$ or k and $\phi = t$, u, v, or c) in equations (7)–(11) for each case (elliptic, parabolic, and boundary layer) are listed in Table 1.

Method of solution

In the calculation grid, the axial velocity components, pressure and temperatures were evaluated at the center of each control volume while the radial velocity components were evaluated at the control volume boundaries. The sequence of calculation steps for cases II and III is as follows.

Step 1. At each axial location equation (10) was solved for the temperature profile ($T_{i,k}$; $k = 1, n+2$). These temperatures were used to determine the fluid thermophysical properties for updating various dimensionless numbers (Re_k, Pe_k) and also evaluating the buoyant force term, y_k^u, in equation (8).

Table 1. Tri-diagonal coefficients used in equations (7)–(10)

I. *Elliptic equations* (*case* I)

$F_{l\pm1/2} = (RV)^{m-1}_{il\pm1/2}/2R_l\Delta R$; $E_l = 1/Re_l(\Delta X)^2$

$G_{l\pm1/2} = (2R)_{l\pm1/2}/R_l(\Delta R)^2$; $H_l^{\pm} = (2R)_l/R_{l\pm1/2}(\Delta R)^2$

(a) Energy equation ($2 \leqslant k \leqslant n+1$)

$a_k^t = -(F + G/Pe)_{k-1/2}$

$b_k^t = U_{i,k}^{m-1}/\Delta X - a_{k+1}^t - c_{k-1}^t$

$c_k^t = (F - G/Pe)_{k+1/2}$

$y_k^t = (UT)_{i-1,k}/\Delta X$

(b) Axial momentum equation ($2 \leqslant k \leqslant n+1$)

$a_k^u = -(F + G/Re)_{k-1/2}$

$b_k^u = U_{i,k}^{m-1}/\Delta X - a_{k+1}^u - c_{k-1}^u + E_{i-1}$

$c_k^u = (F - G/Re)_{k+1/2}$

$y_k^{elip} = E_i(U_{i+1,k} - U_{i-1,k}) + E_{i-1}U_{i-2,k}$

$y_k^u = (Gr_q\, T/4Q\, Re^2)_{i,k} + U_{i-1,k}^2/\Delta X + y_k^{elip}$

(c) Radial momentum equation ($2 \leqslant j \leqslant n$)

$a_j^v = -(H_{j-1}^+ + F_{j-1/2})$

$b_j^v = U_{i,j}/\Delta X + F_{j+1/2} - F_{j-1/2} + H_j^+ + H_j^-$

$c_j^v = -(H_{j+1}^- - F_{j+1/2})$

$x_j^v = (UV)_{i-1,j}/2(\Delta X)$

(d) Continuity equation ($2 \leqslant k \leqslant n+1$)

$a_k^c = -(\rho R)_{k-1}/R_{k-1/2}(\Delta R)$

$b_k^c = (\rho R)_k/R_{k-1/2}(\Delta R)$

$c_k^c = 0$

$x_k^c = [(\rho U)_{i,k-1/2} - (\rho U)_{i-1,k-1/2}]\Delta X$

II. Parabolic equations (case II)

$V_{il}^{m-1} = V_{i-1,l}$; $V_{il}^{m-1} = V_{i-1,l}$

$E_l = 0$

III. Boundary layer equations (case III)

$V_{il}^{m-1} = V_{i-1,l}$; $V_{il}^{m-1} = V_{i-1,l}$

$E_l = a_k^v = b_k^v = c_k^v = y_k^v = 0$

Step 2. The axial momentum equation (equation (8)) was solved iteratively in conjunction with the integral continuity equation (equation (11)) for the axial velocity profiles ($U_{i,k}$; $k = 1, n+2$) and an average value of the pressure gradient, $(\hat{c}P/\hat{c}X)_i$.

Step 3. The radial momentum equation (equation (9)) coupled with the continuity equation (equation (7)) was solved iteratively for the radial velocity ($V_{i,j}$; $j = 1, n+1$) and pressure profiles (P_k; $k = 1, n+1$). The iteration scheme used to solve equations (7) and (9) is very similar to the guess correction scheme suggested for pressure correction by Patankar and Spalding [18].

This completes the calculations at one axial location. The calculation procedure, then, marches to the subsequent downstream axial location. At each axial location the criterion for incipient flow instability was examined; the axial location at which this criterion was satisfied was taken as x_{fr}.

In cases II and III the calculations were terminated once x_{fr} was reached, while in case I additional sweeps of the calculation domain were incorporated to increase the accuracy of the solution. In each sweep the same calculation procedures (steps 1–3) were repeated until the corrections for x_{fr} and the axial velocity profile became very small ($X_{fr}^m - X_{fr}^{m-1} < \Delta X$

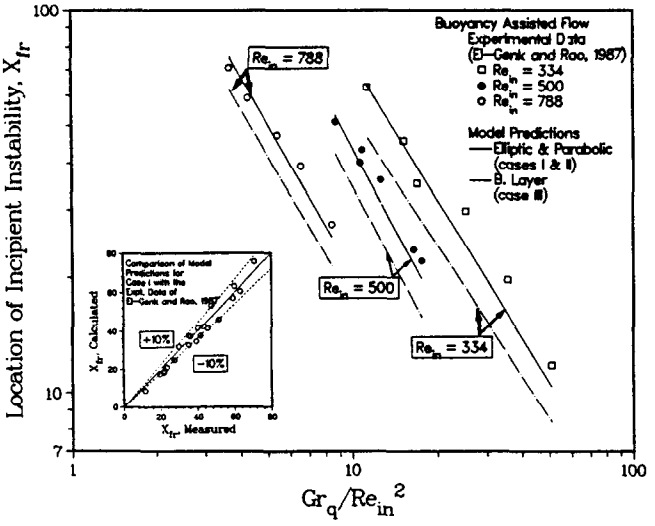

FIG. 2. Comparison of model predictions of X_{fr} for cases I–III with the experimental data for buoyancy assisted flow of water in a vertical annulus having a diameter ratio of 2.

and $U^m - U^{m-1} \leqslant 0.001$). The calculation procedure in case I was initiated by using the model predictions of temperature, axial and radial velocities, and pressure profiles for case II as the starting point during the first sweep. The coefficients in equations (7)–(10) were evaluated and steps 1–3 outlined above were carried out to obtain more accurate estimates of x_{fr} and U, V, T, and P.

The accuracy and convergence of the results obtained using the marching solution scheme described above were very sensitive to the axial and radial step widths [18]. Because conducting a full sensitivity analysis of convergence, stability and accuracy of the solution scheme was beyond the scope of this study, a number of test cases were performed to quantify the effect of varying the control volume widths, ΔX and ΔR, on the accuracy of the results as well as the computation time. Results revealed that for the range of geometrical parameters selected in the study ($\varepsilon = 1.2$–2.0 and $D_i = 1.27$–2.25 cm) a ΔX of 0.05 and ΔR of 0.01 were suitable. When these values were reduced to 0.025 and 0.005, respectively, the computation time increased by 125%, with negligible effect on the numerical results. Hence, subsequent calculations were carried out using the former values of ΔX and ΔR.

RESULTS AND DISCUSSIONS

The accuracy of the model was verified by comparing its predictions of x_{fr} with the experimental data of ref. [4], for both buoyancy assisted and opposed flows, and those of Sherwin and Wallis [14] for buoyancy opposed flow (see Figs. 2–4). In addition, the contributions of the axial momentum diffusion and of the radial momentum transfer were assessed by comparing the model predictions of case I with those of case II and case III, using the parabolic equations and the boundary layer equations, respectively.

As shown in Figs. 2 and 3, the model predictions of x_{fr} in cases I and II are very similar and in reasonable agreement with the experimental data of ref. [4] for buoyancy assisted flow (within $\pm 10\%$). However, for buoyancy opposed flow the experimental values of x_{rf} are up to 15% higher than the model predictions (see Fig. 3). These higher experimental values of x_{rf} can be attributed to the experimental uncertainties, up to 20%, in measuring x_{fr} for buoyancy opposed flow. These uncertainties were due to the fact that while the onset of instability occurred near the inner heated wall the dye solution was injected near the outer wall, hence delaying the detection of flow instability. On the other hand, in the buoyancy assisted flow experiments the uncertainties in x_{fr} measurements were smaller than for downflow ($\pm 10\%$) because the onset of flow instability occurred near the outer wall where the dye solution was injected into the flow.

Figure 4 compares the model predictions for x_{fr} with the experimental data of Sherwin and Wallis [14] for buoyancy opposed flow in a vertical annulus having a diameter ratio of 3.0. Because the inlet water temperature for the individual data points was not reported, a point-by-point comparison with the data was not possible. Instead the model predictions of x_{fr} in Fig. 4 were obtained by assuming constant water properties. As the results in Fig. 4 demonstrate, while the model predictions in cases I and II were in reasonable agreement ($\pm 12\%$) with the experimental data, those obtained using the boundary layer approximation (case III) were consistently lower, with the difference increasing with decreasing x_{fr} (or increasing Gr_q/Re).

In Figs. 2–4, the almost identical predictions of x_{fr} by both the elliptic and parabolic equations (cases I

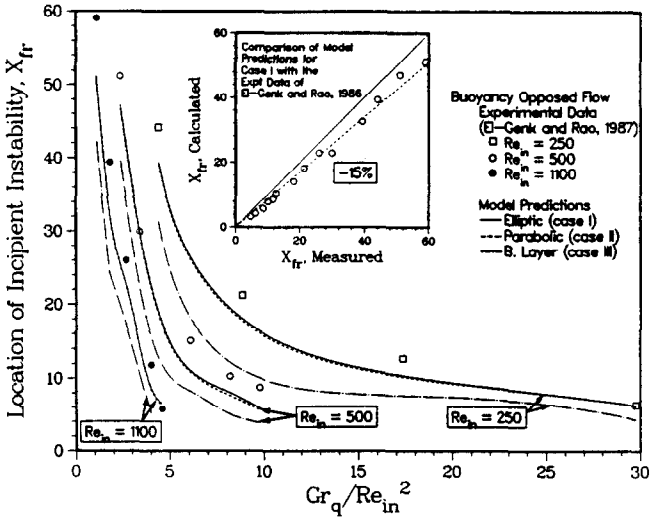

FIG. 3. Comparison of model predictions of X_{fr} for cases I–III with the experimental data for buoyancy opposed flow of water in a vertical annulus having a diameter ratio of 2.

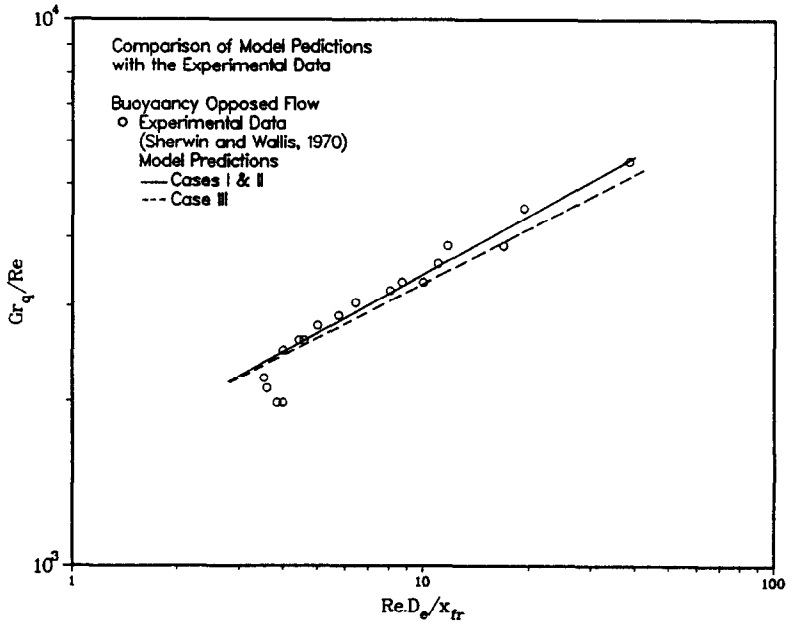

FIG. 4. Comparison of model predictions of X_{fr} for cases I–III with the experimental data for buoyancy opposed flow of water in a vertical annulus having a diameter ratio of 3.

and II) demonstrate that the effect of axial momentum diffusion on x_{fr} is negligible. However, from the numerical solution point of view the elliptic form of governing equations was preferred because the solution remained stable until the matrix equation became singular a few centimeters downstream of x_{fr}.

The effect of radial momentum transfer on x_{fr} was determined by comparing the model predictions for case III with those for case I (see Figs. 2 and 3). As Figs. 2 and 3 indicate, the boundary layer solution (case III) underpredicts x_{fr} for buoyancy assisted and opposed flows by 20–40% and 25–45%, respectively. These lower values of x_{fr} are due to the fact that the boundary layer equations neglect the contribution of radial momentum transfer to the development of the velocity fields, which could be significant at higher Gr_q/Re ratios. As shown in Figs. 5 and 6, the difference between the axial velocity profiles in cases I and III is negligible near the entrance ($X = 2.25$ and 12.5 in Figs. 5 and 6), where the effect of buoyant forces is insignificant. However, as the contribution of buoyant forces increases with axial distance, the difference between the axial velocity profiles in cases I and III increases. As Figs. 5 and 6 show neglecting the radial momentum transfer in case III overpredicted the values of the axial velocity in the region adjacent to

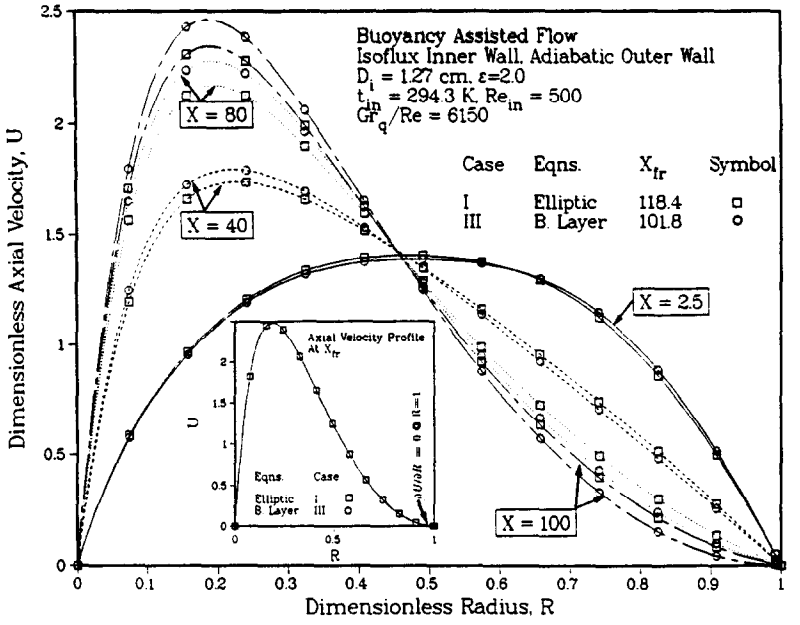

FIG. 5. Comparison of model predictions of axial velocity at various axial locations for cases I–III for $Gr_q/Re = 6150$.

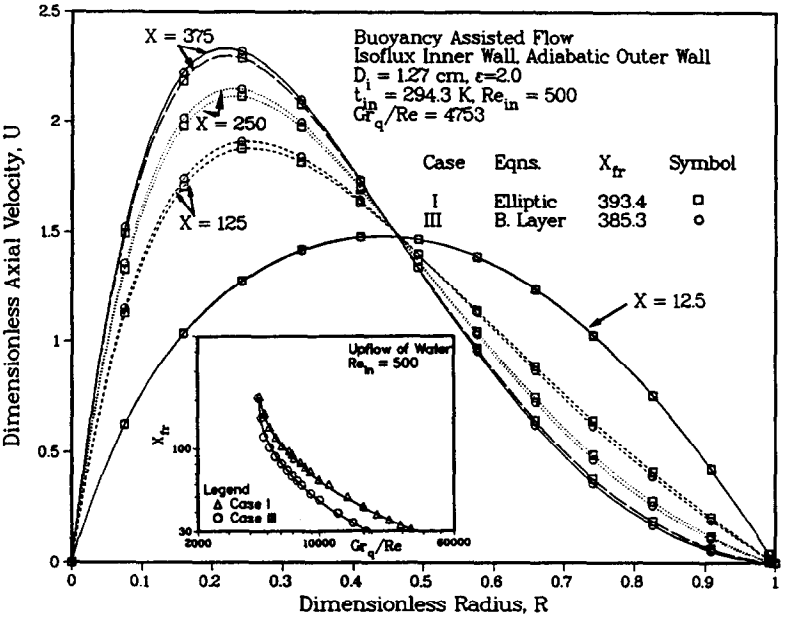

FIG. 6. Comparison of model predictions of axial velocity at various axial locations for cases I–III for $Gr_q/Re = 4753$.

the heated wall, hence resulting in earlier prediction of incipient instability. The insert in Fig. 5 illustrates that the axial velocity profile at the location of incipient instability, which met the onset of flow instability criterion ($\partial U/\partial R = 0$ @ $R = 1$), was identical for cases I and III. As Fig. 6 shows, at lower Gr_q/Re values ($Gr_q/Re < 5000$) the deviation between the model prediction of x_{fr} for cases I and III is less than 7%, but is as much as 50% at a Gr_q/Re of 40 000. In summary, the results presented in Figs. 2–6 clearly show that while the contribution of the axial diffusion of momentum to x_{fr} is insignificant, the contribution of the radial momentum transfer is important, particularly at higher Gr_q/Re values. At these values either the elliptic or the parabolic form of equations should be used to describe the flow field.

In the following sections a parametric analysis is conducted using the elliptic form of the governing

equations (case I) to assess the effects of inlet parameters, operating parameters, and geometrical parameters on x_{fr}.

Effect of inlet axial velocity profile

The effect of inlet axial velocity profile on x_{fr} is assessed by assuming a flat axial velocity profile at the inlet of the annulus and varying the length of the non-heated calming section, L_{nh}, that preceded the heated part of the annulus. The value of L_{nh} is varied from $10D_e$ to $500D_e$; which at Re_{in} of 500 corresponds to 25–99% hydrodynamically developed isothermal velocity profiles at the inlet to the heated section, respectively.

Results in Fig. 7 show that for Gr_q/Re values larger than 5000 varying the inlet axial velocity profile only insignificantly affects the model predictions of x_{fr}, which increase with Re_{in}. However, for $Gr_q/Re < 5000$ the values of x_{fr} are independent of both the inlet velocity profiles and Re_{in}. For Gr_q/Re values less than 5000 very few cases were performed because the associated values of x_{fr} were very large, requiring large computational effort. The results delineated in the insert in Fig. 7 explain the lack of dependence of x_{fr} on the axial velocity profile at the inlet of the heated section. As this figure shows, although the axial velocities at the entrance corresponding to $L_{nh} = 0$ and 200 are distinctly different due to the effect of buoyancy they became identical for $X \geqslant 15$ resulting in identical predictions of x_{fr} for both cases.

Effect of operating parameters

The operating parameters of interest in the present study are Gr_q/Re, and inlet temperature. The model predictions for both buoyancy assisted and opposed flows are plotted in Figs. 8 and 9, respectively. As is evident from these figures when the water properties are evaluated at the local bulk temperature, the model predictions of x_{fr} for a wide range of operating conditions collapse into essentially a single line. Conversely, when the water physical properties are evaluated at the inlet temperatures the values of x_{fr} do not collapse into a single line.

Figures 8 and 9 suggest that for given Re and Pr the values of x_{fr} increase with decreasing Gr_q/Re until a critical value $(Gr_q)_{cr}$ below which the flow is unconditionally stable ($x_{fr} \to \infty$). The values of $(Gr_q/Re)_{cr}$ for buoyancy assisted and opposed flows were found to be 3850 and 1500, respectively (see Figs. 8 and 9). These values are in good agreement with those reported by Sherwin [12] for fully developed flows. Also, the results in Figs. 8–10 show that the values of $(Gr_q/Re)_{cr}$ are independent of not only the inlet and operating conditions but also the geometrical parameters.

Effect of geometrical parameters

To examine the effects of both the equivalent diameter, D_e, of the annulus and the annulus ratio, ε, on X_{fr}, a parametric analysis was performed using the geometrical parameters shown in Fig. 10. As this figure shows, the values of X_{fr} increase as either D_i or the annulus ratio increases. The insert in Fig. 10 also shows that the effects of various geometrical parameters can be accounted for by plotting the results in terms of x_{fr}/D_e vs $Gr_q/(\varepsilon+1)Re$. Consequently, these dimensionless quantities are used in the next section to develop a general criteria for incipient flow instability in annular geometries (see Fig. 11).

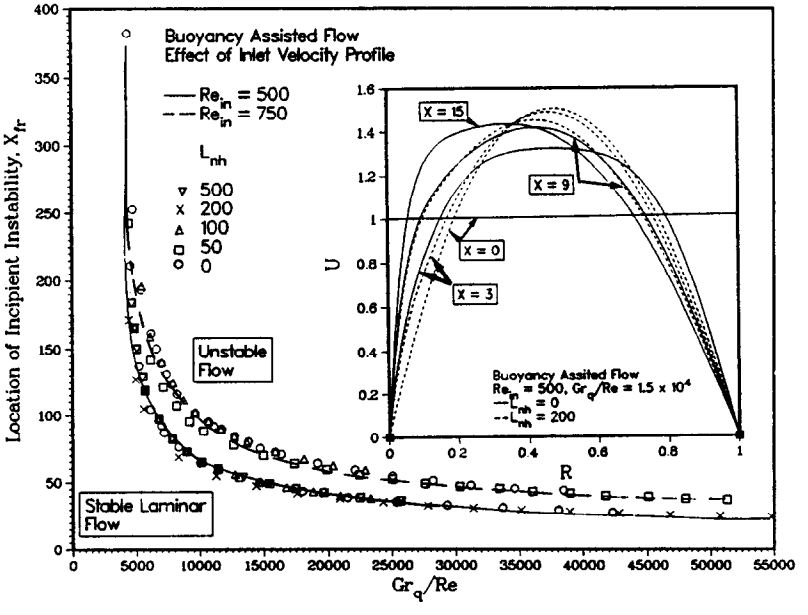

FIG. 7. Effect of inlet axial velocity profile on the location of incipient flow instability for buoyancy assisted flow in a uniformly heated vertical annulus having a diameter ratio of 2.

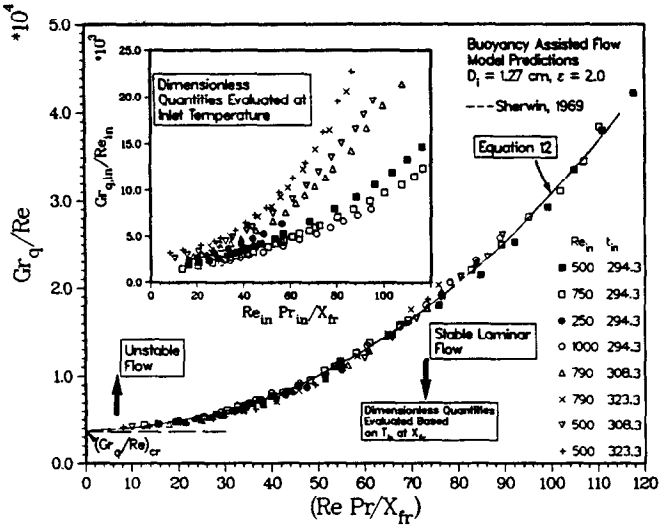

FIG. 8. Effect of operating parameters on the location of incipient flow instability for buoyancy assisted flow in uniformly heated vertical annulus having a diameter ratio of 2.

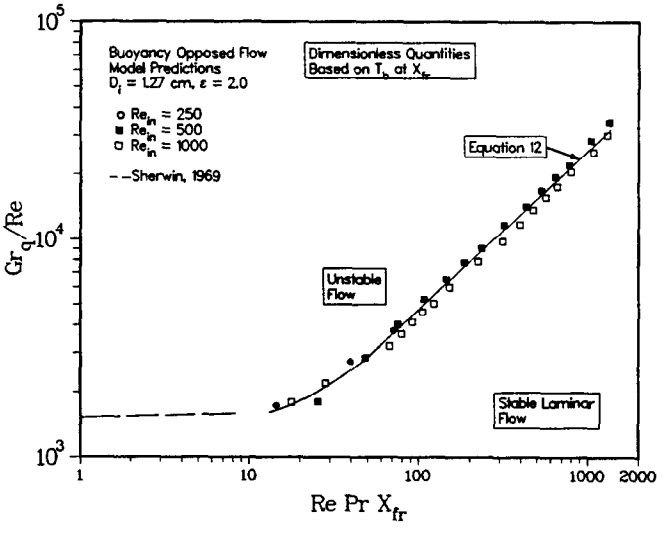

FIG. 9. Effect of operating parameters on the location of incipient flow instability for buoyancy opposed flow in uniformly heated vertical annulus having a diameter ratio of 2.

Flow instability criteria for annular geometries

Based on the model predictions of x_{fr} for both buoyancy assisted and opposed flows using various operating and geometrical conditions, as well as the experimental data of refs. [4, 14], the following criteria for incipient flow instability were suggested:

$$[Gr_q/Re-(Gr_q/Re)_{cr}] = A(Re\ Pr\ D_e/x_{fr})^b(\varepsilon+1) \quad (12)$$

where $(Gr_q/Re)_{cr} = 3850$, $A = 0.18$, and $b = 2.32$ for upflow and $(Gr_q/Re)_{cr} = 1500$, $A = 15.15$, and $b = 0.90$ for downflow.

These criteria are compared in Figs. 8 and 10 with the model predictions for buoyancy assisted flows for different operating and geometrical parameters, respectively. A similar comparison of these criteria with the model predictions and the experimental data for buoyancy opposed flow is shown in Figs. 9 and 11, respectively. Figure 11 also provides a comparison of these criteria with the experimental data for buoyancy assisted flow. Note the good agreement between the data and equation (12) (within ±15 and ±11% for buoyancy opposed flow and assisted flow, respectively).

Based on this agreement with the experimental data, equation (12) is proposed to demarcate laminar and buoyancy induced turbulent flows in vertical annuli having a uniformly heated inner wall and an adiabatic outer wall. For a selected Graetz number $(Re\ Pr\ D_e/x_{fr})$, the flow would be either stable or unstable depending on whether the Gr_q/Re values are lower or higher than those predicted by equation (12), respectively.

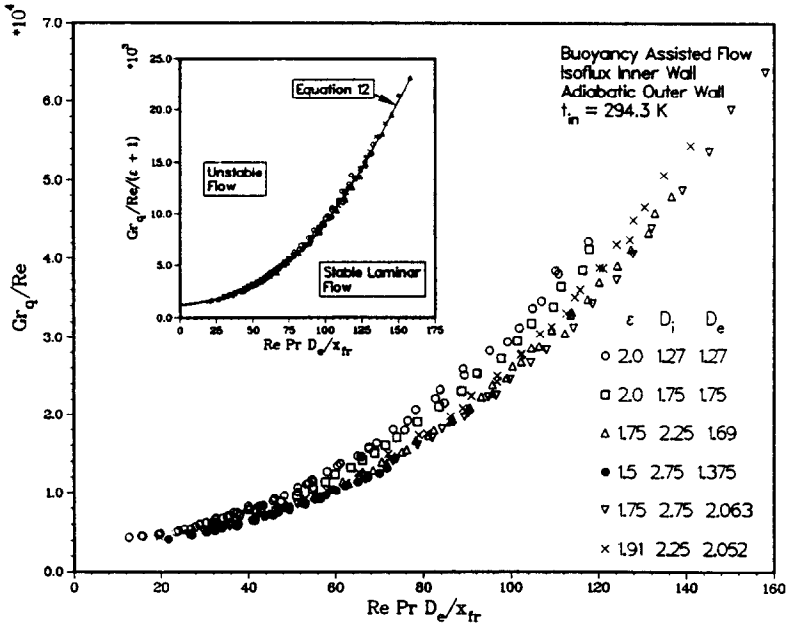

FIG. 10. Effect of geometrical parameters on the location of incipient flow instability for buoyancy assisted flow in uniformly heated vertical annuli.

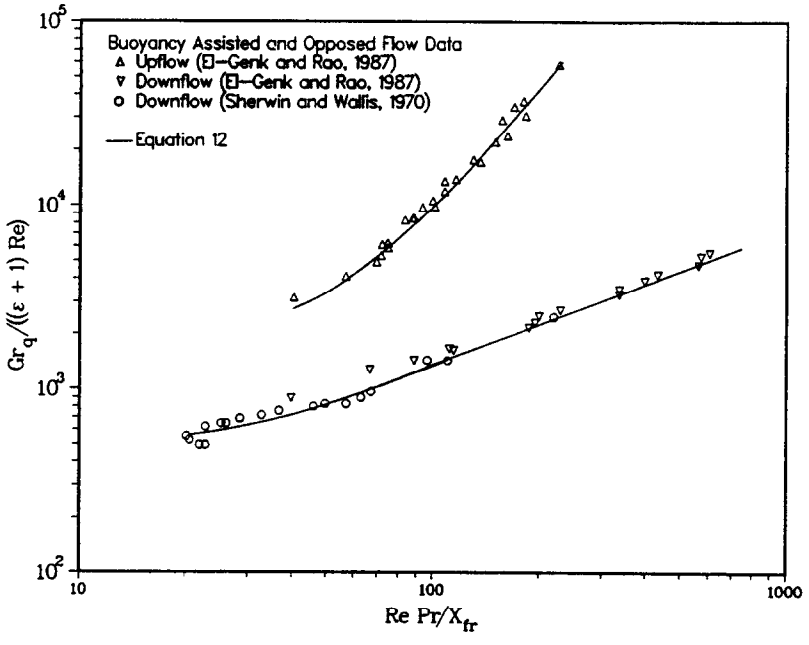

FIG. 11. Comparison of the criteria for onset of flow instability with the experimental data for both buoyancy assisted and opposed flows.

CONCLUSIONS

A two-dimensional numerical model based on the elliptic Navier–Stokes equations was developed to predict the location of incipient instability, X_{fr}, for low Reynolds number water flows in vertical annuli. The model predictions for X_{fr} were in good agreement with the experimental data of ref. [4], for buoyancy assisted and opposed flow, and Sherwin and Wallis [14] for buoyancy opposed flow.

To assess the effects of axial momentum diffusion and radial momentum transfer on the accuracy of the model prediction of x_{fr}, the research also solved the parabolic form of the Navier–Stokes equations and the boundary layer equations for x_{fr}. Results showed that while the boundary layer approximation can

adequately describe the flow field at very low Gr_q/Re values, it significantly underestimates x_{fr} at higher Gr_q/Re because of neglecting the radial momentum transfer. Conversely, the results revealed that the axial diffusion of momentum only insignificantly affects the axial velocity profiles and, hence, the prediction of the location of incipient flow instability. In conclusion, either the elliptic or parabolic form of Navier–Stokes equations would accurately predict the onset of flow instability. However, the former is preferred because the numerical solution remained stable until the matrix equations became singular a few centimeters downstream of x_{fr}.

A general criteria (equation (12)) for predicting the onset of flow instability in vertical annuli having an isoflux inner wall and an adiabatic outer wall was developed based on both the model predictions and the experimental data of ref. [4, 14]. These criteria were in good agreement with the experimental data of ref. [4] and of Sherwin and Wallis [14] for annular ratios of 2.0 and 3.0, respectively. Equation (12) is, therefore, recommended for demarcating the laminar and buoyancy induced turbulent flows in vertical annuli.

REFERENCES

1. B. Gebhart and R. L. Mahajan, Instability and transition in buoyancy-induced flows, *Adv. Appl. Mech.* **22**, 231–315 (1982).
2. G. F. Sheele and H. L. Greene, Transition to turbulent behavior in non-isothermal pipe flow, *A.I.Ch.E. Jl* **12**(4), 737–740 (1966).
3. T. E. Mullin and E. R. Gergard, Heat transfer to water in downward flow in a uniform wall temperature vertical tube at low Graetz numbers, *J. Heat Transfer* **99**, 586–592 (1977).
4. M. S. El-Genk and D. V. Rao, Buoyancy induced instability of laminar flows in vertical annuli—I. Flow visualization and heat transfer experiments, *Int. J. Heat Mass Transfer* **33**, 2145–2159 (1990).
5. T. J. Hanratty, E. M. Rosen and R. L. Kabel, Effect of heat transfer on flow field at low Reynolds numbers in vertical tubes, *Ind. Engng Chem.* **50**(5), 815–820 (1958).
6. E. M. Rosen and T. J. Hanratty, Use of boundary layer theory to predict the effect of heat transfer on the laminar flow field in a vertical tube with a constant temperature wall, *A.I.Ch.E. Jl* **7**(1), 112–123 (1961).
7. T. M. Hallman, Experimental study of combined forced and free convection in a vertical tube, NASA Technical Report, No. D-104 (1961).
8. J. W. Yang, Heat transfer and fluid flow in regular rod arrays with opposing flow. In *Fluid Flow and Heat Transfer Over Rod or Tube Bundles* (Edited by S. C. Yao and P. A. Pfund), pp. 149–153. ASME, New York (1979).
9. V. Iannello, K. Y. Suh and N. E. Todreas, Mixed convection friction factors and Nusselt numbers in vertical annular and subchannel geometries, *Int. J. Heat Mass Transfer* **31**, 2175–2189 (1988).
10. E. M. Sparrow, G. M. Chrysler and L. F. Azevado, Observed flow reversal and measured-predicted Nusselt numbers for natural convection in a one-sided heated vertical channel, *J. Heat Transfer* **106**, 325–332 (1984).
11. R. A. Wirtz and P. McKinley, Boundary effect on downward laminar convection between parallel plates. In *Fundamentals of Forced and Mixed Convection* (Edited by F. A. Kulacki and R. D. Boyd), HTD-Vol. 42. ASME, New York (1985).
12. K. Sherwin, Combined natural and forced laminar flow in vertical annuli, *Br. Chem. Engng* **14**(9), 1215–1217 (1969).
13. J. H. Kim, Analysis of laminar mixed convection in a vertical tube annulus with upward flow. In *Fundamentals of Forced and Mixed Convection* (Edited by F. A. Kulacki and R. D. Boyd), HTD-Vol. 42, pp. 91–98. ASME, New York (1985).
14. K. Sherwin and J. D. Wallis, A theoretical study of combined natural and forced laminar convection for developing flow down vertical annuli, *Fourth Int. Heat Transfer Conf.*, Vol. IV, Paper No. Nc 3.9, Paris (1970).
15. M. A. I. El-Shaarawi and A. Sharan, Free convection effects on the developing laminar flow in concentric vertical annuli, *J. Heat Transfer* **102**, 617–622 (1980).
16. S. V. Patankar, A calculation procedure for two-dimensional elliptic situations, *Numer. Heat Transfer* **4**, 409–425 (1981).
17. J. P. Van Doormaal and G. D. Raithby, Enhancements of the SIMPLE method for predicting incompressible fluid flows, *Numer. Heat Transfer* **7**, 147–163 (1984).
18. S. V. Patankar and D. B. Spalding, A calculation procedure for heat, mass, and momentum transfer in three-dimensional parabolic flows, *Int. J. Heat Mass Transfer* **15**, 1787–1805 (1972).
19. F. M. Harlow and A. A. Amsden, Fluid dynamics: an introductory text, Report No. LA-4100, Los Alamos Scientific Laboratory, Los Alamos, New Mexico (1970).

INSTABILITE INDUITE PAR FLOTTEMENT POUR DES ECOULEMENTS LAMINAIRES DANS UN ESPACE ANNULAIRE VERTICAL—II. MODELE DU DEVELOPPEMENT ET ANALYSE

Résumé—Un modèle numérique bidimensionnel, basé sur les équations elliptiques de Navier–Stokes, est développé pour prédire l'emplacement de l'apparition de l'instabilité, x_{fr}, dans des écoulements d'eau à faible nombre de Reynolds dans des espaces annulaires verticaux. Les résultats montrent que si la quantité de mouvement radiale est négligée les valeurs de x_{fr} sont sous-évaluées de 45% environ pour des valeurs élevées du rapport Gr_q/Re. Par contre la diffusion axiale de quantité de mouvement affecte peu le champ des vitesses et par suite la précision du calcul de x_{fr}. Les résultats de l'analyse paramétrique étudiant les effets de diverses conditions opératoires et des paramètres géométriques sont utilisés pour développer des critères généraux de prédiction de l'apparition de l'instabilité de l'écoulement dans des espaces annulaires verticaux. Ces critères conviennent à ± 10 et $\pm 15\%$ aux données expérimentales, respectivement pour des écoulements aidés ou contrariés par le flottement.

AUFTRIEBSINDUZIERTE INSTABILITÄT EINER LAMINAREN STRÖMUNG IN EINEM SENKRECHTEN RINGKANAL—II. MODELLBILDUNG UND ANALYSE

Zusammenfassung—Es wird ein zweidimensionales numerischen Modell vorgestellt, das auf den elliptischen Navier–Stokes-Gleichungen aufbaut und den Ort des Einsetzens der Instabilität (x_{ft}) in einem senkrechten, wasserdurchströmten Ringkanal (kleine Reynolds-Zahlen) berechnet. Die Ergebnisse zeigen, daß x_{ft} durch Vernachlässigen des radialen Impulses bei großen Werten von Gr_q/Re um bis zu 45% zu klein berechnet wird. Andererseits beeinflußt der axiale Impulsaustausch das Geschwindigkeitsfeld nur unwesentlich und damit auch die Genauigkeit der Berechnung von x_{ft}. In einer Parameteruntersuchung werden die Einflüsse unterschiedlicher Arbeitsbedingungen und unterschiedlicher geometrischer Bedingungen untersucht. Mit Hilfe des Ergebnisses lassen sich allgemeine Kriterien für die Berechnung des Einsetzens der Strömungsinstabilität in senkrechten Ringkanälen entwickeln. Versuchsergebnisse für auftriebsunterstützte und auftriebsbehinderte Strömungen können mit Hilfe dieser Kriterien innerhalb ± 10 bzw. $\pm 15\%$ wiedergegeben werden.

НЕУСТОЙЧИВОСТЬ ЛАМИНАРНЫХ ТЕЧЕНИЙ В ВЕРТИКАЛЬНЫХ КОЛЬЦЕВЫХ КАНАЛАХ, ВЫЗВАННАЯ ПОДЪЕМНЫМИ СИЛАМИ—II. РАЗРАБОТКА МАТЕМАТИЧЕСКОЙ МОДЕЛИ И АНАЛИЗ РЕЗУЛЬТАТОВ

Аннотация—На основе эллиптических уравнений Навье–Стокса разработана двумерная численная модель для определения места возникановения неустойчивости x_{ft} в воде при малых значениях числа Рейнольдса в вертикальных кольцевых каналах. Результаты показывают, что пренебрежение радиальным импульсом межот привести к занижению значений x_{ft} на 45% при высоких значениях Gr_q/Re. Аксиальная же диффузия импульса лишь незначительно влияет на поля скоростей и, следовательно, на точность расчета значения x_{ft}. Результаты параметрического анализа эффектов различных рабочих условий и геометрических параметров используются для установления общих критчриев определения неустойчивости течения в вертикальных кольцевых каналах. Расхождения между установленными критериеми и экспериментальными даными составляют ± 10 и $\pm 15\%$ соответственно для течений с совпадающим и противоположным действием подъемных сил и вынужденного течения.